

Dopant-Free, Amorphous–Crystalline Heterophase SnO₂ Electron Transport Bilayer Enables >20% Efficiency in Triple-Cation Perovskite Solar Cells

Hock Beng Lee, Neetesh Kumar, Manoj Mayaji Ovhal, Yeong Jae Kim, Young Min Song, and Jae-Wook Kang*

Improving the ohmic contact and interfacial morphology between an electron transport layer (ETL) and perovskite film is the key to boost the efficiency of planar perovskite solar cells (PSCs). In the current work, an amorphous–crystalline heterophase tin oxide bilayer (Bi-SnO₂) ETL is prepared via a low-temperature solution process. Compared with the amorphous SnO₂ sol–gel film (SG-SnO₂) or the crystalline SnO₂ nanoparticle (NP-SnO₂) counterparts, the heterophase Bi-SnO₂ ETL exhibits improved surface morphology, considerably fewer oxygen defects, and better energy band alignment with the perovskite without sacrificing the optical transmittance. The best PSC device (active area ≈ 0.09 cm²) based on a Bi-SnO₂ ETL is hysteresis-less and achieves an outstanding power conversion efficiency of $\approx 20.39\%$, which is one of the highest efficiencies reported for SnO₂-triple cation perovskite system based on green antisolvent. More fascinatingly, large-area PSCs (active areas of ≈ 3.55 cm²) based on the Bi-SnO₂ ETL also achieves an extraordinarily high efficiency of $\approx 14.93\%$ with negligible hysteresis. The improved device performance of the Bi-SnO₂-based PSC arises predominantly from the improved ohmic contact and suppressed bimolecular recombination at the ETL/perovskite interface. The tailored morphology and energy band structure of the Bi-SnO₂ has enabled the scalable fabrication of highly efficient, hysteresis-less PSCs.

1. Introduction

In the past decade, organic–inorganic lead halide perovskite solar cells (PSCs) have been the main focus of research in both academic institutions and photovoltaic industry because of their excellent optoelectronic properties and low materials and fabrication costs. With the optimization of the fabrication methods and

device configurations, laboratory-scale PSCs have achieved a power conversion efficiency (PCE) as high as 25.2%, which is on-par with that of conventional crystalline silicon solar cells.^[1–3] As a critical part of device configuration, electron transport layers (ETLs) play an essential role in charge separation, electron transport, and hole-blocking in PSC devices. Numerous research outcomes have demonstrated that the energy band alignment and interfacial charge recombination between the ETL and perovskite layer exert a significant impact on the device performance.^[4–7] Therefore, it is pre-requisite to develop an ETL with tailored morphology, optoelectronic properties, and compatible band alignment with perovskite, in order to fabricate high performance PSCs.


In the early stages of research, compact-mesoporous heterophase titanium dioxide (TiO₂) was widely used as the ETL in n-i-p structure PSCs due to its excellent electron selectivity.^[8–10] However, the high-temperature fabrication route (>450 °C), low conductivity, and strong photo-oxidation of TiO₂ under solar irradiation make it an undesirable ETL for PSCs in the long run.^[10]

To alleviate these problems, low-temperature processable (<185 °C) metal oxide (MO) ETLs with fewer photocatalytic effects were introduced, such as zinc oxide (ZnO),^[11] tungsten trioxide (WO₃),^[12] niobium oxide (NbO_x),^[13] cerium oxide (CeO_x),^[14] ferric oxide (Fe₂O₃),^[15] tin oxide (SnO₂),^[16] and silicon dioxide (SiO₂).^[17] SnO₂, in particular, was extensively investigated due to its high optical transparency, electron mobility (240 cm²V^{−1}s^{−1}), charge selectivity, and low-temperature processability.^[18–21] More importantly, SnO₂ has an inherently compatible energy level alignment with lead-halide perovskite, that is, a conduction band (CB) edge slightly lower than that of the perovskite to facilitate electron extraction and a valence band (VB) edge much lower than that of the perovskite to block the holes.^[22] These interesting features altogether make SnO₂ a viable ETL to replace its predecessor, TiO₂ in PSCs.

Most of the MO-based ETLs, including SnO₂, exhibit an attenuated electron conductivity and carrier diffusion coefficient due to the defect-induced charge trapping-detrapping phenomenon.^[23] To improve the inherent electronic and

Dr. H. B. Lee, Dr. N. Kumar, M. M. Ovhal, Prof. J.-W. Kang
Department of Flexible and Printable Electronics
LANL-CBNU Engineering Institute-Korea
Chonbuk National University
Jeonju 54896, Republic of Korea
E-mail: jwkang@jbnu.ac.kr

Dr. Y. J. Kim, Prof. Y. M. Song
School of Electrical Engineering and Computer Science
Gwangju Institute of Science and Technology
123 Cheomdangwagi-ro, Buk-gu, Gwangju 61005, Republic of Korea

 The ORCID identification number(s) for the author(s) of this article can be found under <https://doi.org/10.1002/adfm.202001559>.

DOI: 10.1002/adfm.202001559

interfacial properties of SnO_2 ETLs, strategies that include compositional engineering and heteroatom doping have been commonly practiced. There are previous reports detailing the heteroatom doping of SnO_2 through the replacement of the Sn^{4+} ions with different elements, including Li,^[24] Mg,^[25] Nb,^[26] Zn,^[27] Zr,^[28] and Y^[29] to enhance its optoelectronic properties and modify its electronic band structure. Each of these doping attempts has yielded a considerable improvement in the PCE of PSCs. Nonetheless, it is widely acknowledged that doping is a double-edged sword, whereby an insufficient dopant concentration yields limited improvement, while a superfluous dopant concentration adversely affects the device performance. It is also highly challenging to precisely control the doping density in the host material and there is a lack of measures to ensure the reproducibility of doping. Furthermore, most of the dopant atoms remain electrically active in the host lattice and they are likely to diffuse out from the host lattice to interfacial boundaries under the influence of voltage bias, thereby deteriorating the stability of the entire PSC device system.

Apart from heteroatom doping, another effective approach to modify the energy band structure and defect-states of the SnO_2 ETL is via surface morphology optimization. The morphology and crystallography of the SnO_2 ETL are key factors that determine the PSC device performance. A conventional sol–gel based SnO_2 film (SG- SnO_2), prepared via the sol–gel approach, was reported to be amorphous in nature and exhibits severe surface and morphological defects, such as many pinholes and voids that cause inferior device performance with poor reproducibility.^[30,31] To address this issue, heterostructured ETLs composed of different binary MOs have been designed. For instance, Lee et al. fabricated planar PSCs on an amorphous TiO_2 /crystalline SnO_2 ETL, resulting in a PCE of 19.8%.^[32] Liu et al. reported compact TiO_2 / SnO_2 dual ETLs for PSCs, and achieved a PCE of 18% for their devices.^[33] Wang et al. obtained a PCE of 18% for PSCs based on ZnO/crystalline SnO_2 ETLs.^[34] Ma et al. deposited an inorganic ultrathin nanocrystalline MgO hole-blocking layer on the anode surface and the resulting MgO/ SnO_2 -based PSC yielded a PCE of over 18%.^[35] The concept of heterostructured ETLs appears to be the key to boosting the performance of PSCs.

In this work, we introduce a facile, sequential spin-coating method to prepare a dopant-free, amorphous–crystalline heterophase SnO_2 bilayer (Bi- SnO_2) ETL. The Bi- SnO_2 exhibits improved morphology, quenched defects, and better energy level alignment with the perovskite than the widely used SG- SnO_2 . Basically, the Bi- SnO_2 ETL is the hybrid of the amorphous SG- SnO_2 and crystalline SnO_2 nanoparticles (NP- SnO_2), in which the NP- SnO_2 functions as a scaffold atop the SG- SnO_2 film to suppress its surface defects and alter its energy band structure. Therefore, the resulting heterophase Bi- SnO_2 ETL simultaneously exhibits the unique features of both amorphous SG- SnO_2 and crystalline NP- SnO_2 . The mechanism of the interfacial charge transport and recombination of PSCs employing different types of SnO_2 ETLs have been systematically investigated to clarify the influence of the ETL-perovskite interfacial morphology on the eventual PSC device performance. The results show that the Bi- SnO_2 ETL can inhibit the undesirable contact between the ITO and the perovskite film more effectively than the SG- SnO_2 ETL. Simultaneously, Bi- SnO_2 ETL also exhibits a morphology with a higher surface-area-to-volume

ratio than that of the NP- SnO_2 film, which provides a larger ETL-perovskite interfacial contact area for electron extraction. As a result, the champion Bi- SnO_2 -based PSC (active area $\approx 0.09 \text{ cm}^2$) achieved a PCE of $\approx 20.39\%$, which is significantly higher than the PCEs of the SG- SnO_2 and NP- SnO_2 counterparts and rivals with the PCEs of state-of-the-art SnO_2 -triple cation PSCs reported in the literature (Table S1, Supporting Information). A further application of the Bi- SnO_2 ETL to a large-area PSC (active area $\approx 3.55 \text{ cm}^2$) has successfully boosted its PCE from $\approx 12.23\%$ up to $\approx 14.93\%$. Most importantly, there are negligible hysteresis in both small-area and large-area PSCs based on Bi- SnO_2 ETLs. The dopant-free, amorphous–crystalline heterophase Bi- SnO_2 is an ideal ETL for the scalable fabrication of PSCs with outstanding performance and efficiency.

2. Results and Discussions

The surface topographies of the nanostructured SG- SnO_2 , NP- SnO_2 , and Bi- SnO_2 films on ITO substrates were characterized using an atomic force microscopy (AFM). The 2D-AFM micrograph in Figure 1a shows that the surface of the SG- SnO_2 film is uniformly covered with a high density of dome-shaped nanostructures (nanodomains), with visible voids among the nanodomains. These nanodomains are irregular in size, have a lateral dimension in the range of 0.1–1.0 μm and a vertical dimension of $\approx 30 \text{ nm}$. Despite the relatively wide lateral diameters of the nanodomains, the surface of the SG- SnO_2 film only has an r.m.s. roughness of $\approx 775 \text{ nm}$. On the other hand, the NP- SnO_2 film exhibits an entirely different topography. As presented in Figure 1b, the NP- SnO_2 film has a highly compact, pinhole-free, and ultrasmooth surface, with an r.m.s. surface roughness of only $\approx 1.33 \text{ nm}$. This is because the NP- SnO_2 film is obtained directly from the coalescence of ultrafine SnO_2 colloidal nanoparticles. The topography of the Bi- SnO_2 film, acquired via the sequential deposition (spin-coating) of SG- SnO_2 film and NP- SnO_2 scaffold, is displayed in Figure 1c. Interestingly, the Bi- SnO_2 film simultaneously exhibits the distinctive features of both parent films, that is, i) the loosely packed, nanodome morphology of the SG- SnO_2 film and ii) densely packed, nanoparticles morphology of the NP- SnO_2 scaffold. The Bi- SnO_2 film also has a much smoother surface (r.m.s. roughness $\approx 4.68 \text{ nm}$) than that of the SG- SnO_2 film, owing to the overlaying NP- SnO_2 scaffold. The 3D-AFM topographic mappings of the three SnO_2 films are provided in Figure S1, Supporting Information. Simultaneously, the high-resolution 2D-AFM micrographs in Figure 1d–f confirmed that the ultrafine nanoparticles from the NP- SnO_2 scaffold not only overlaid the SnO_2 nanodomains, but also filled up the voids among the nanodomains. Based on the AFM micrographs, the topographies of SG- SnO_2 , NP- SnO_2 , and Bi- SnO_2 films are schematically illustrated. As seen from the 3D illustration in Figure 1g), the SG- SnO_2 film has an inherently coarse texture due to the irregular dimensions of the nanodomains. Contrarily, the highly uniform size of the SnO_2 colloidal nanoparticles gives rise to the NP- SnO_2 film with an extremely smooth and fine-textured surface (Figure 1h). In terms of size, the SnO_2 nanoparticle are extremely fine in comparison with the bulky SnO_2 nanodomains, thus making it easy for the nanoparticles

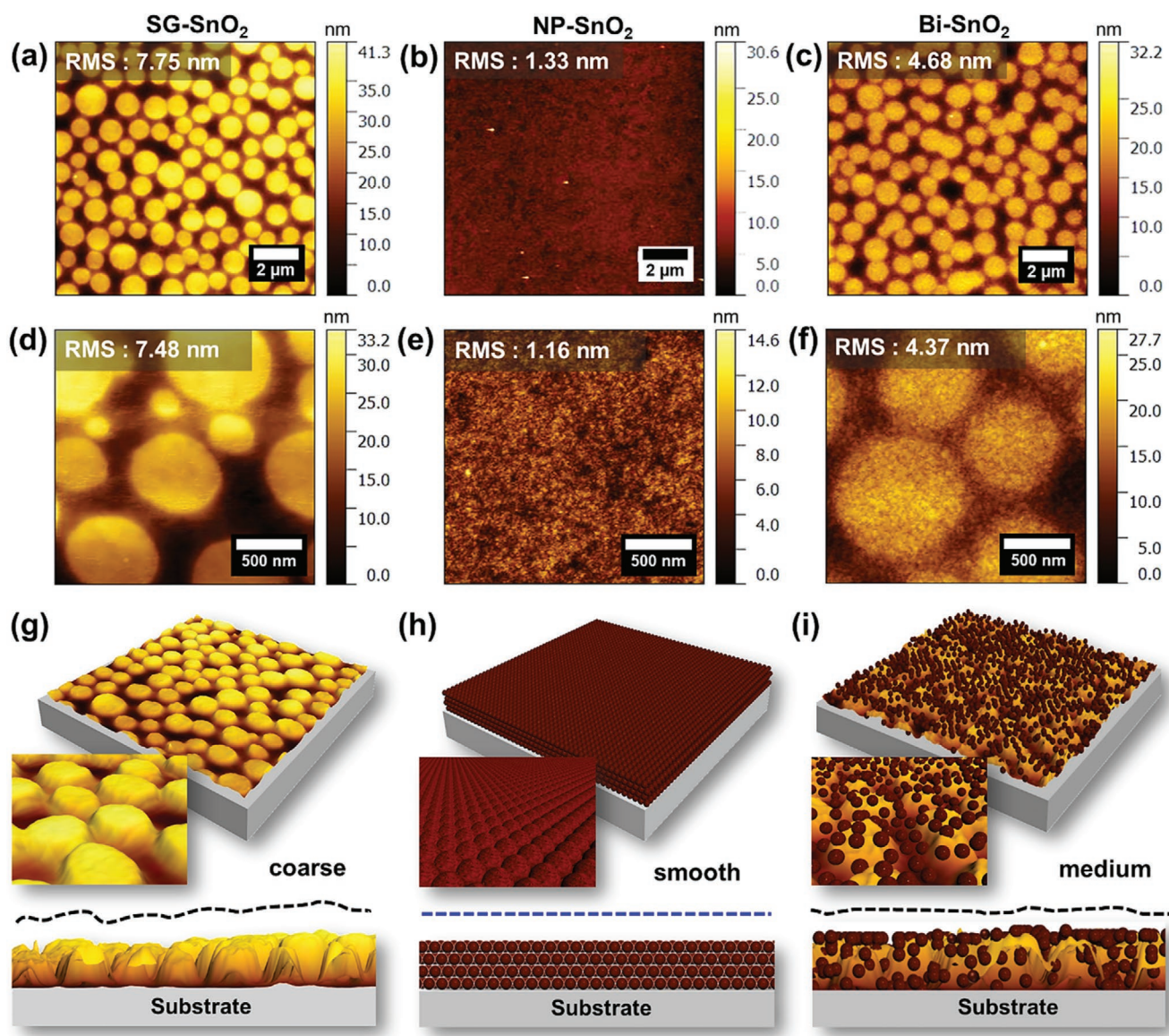


Figure 1. Low-resolution 2D-AFM micrographs of the nanostructured a) SG-SnO₂, b) NP-SnO₂, and c) Bi-SnO₂ films. Corresponding high-resolution 2D-AFM micrographs of the d) SG-SnO₂, e) NP-SnO₂, and f) Bi-SnO₂ films. Schematic diagrams illustrating the surface and cross-sectional views of the g) SG-SnO₂, h) NP-SnO₂, and i) Bi-SnO₂ films.

to infiltrate the SG-SnO₂ film by either filling in the voids among the nanodomains or attaching directly onto the surface of the nanodomains. This yields a Bi-SnO₂ film which exhibits a medium-textured surface with lower roughness with respect to the SG-SnO₂ film (Figure 1i). The effective thicknesses (measured via surface profilometer) of the SG-SnO₂ and NP-SnO₂ films were similar (≈ 30 nm), whereas the thickness of Bi-SnO₂ film was relatively higher (≈ 40 nm).

The morphology of SG-SnO₂ film is further verified via a field-emission scanning electron microscope (FESEM). Figure 2a confirms that the surface of the SG-SnO₂ film is composed of uniformly distributed nanodomains which are irregular in size, with visible voids among the nanodomains. In contrast, the surface of the NP-SnO₂ film is composed of highly compact nanoparticles that yields a void-free morphology (Figure S2,

Supporting Information). These findings agree well with the AFM results. Concurrently, X-ray diffraction (XRD) characterization reveals that the SG-SnO₂ film is amorphous in nature with no obvious diffraction peak (Figure 2b). This finding is already anticipated because typically, an annealing temperature of >450 °C is required to obtain SnO₂ crystallites that yields prominent XRD diffraction peaks. The post-annealing of the SG-SnO₂ film at 190 °C was only intended to accelerate the decomposition of the unstable SnCl₄ phase into the SnO₂ phase, instead of promoting crystallization. Meanwhile, broad diffraction peaks were detected in the XRD pattern of the NP-SnO₂ film, arising primarily from the presence of colloidal nanoparticles in the film. The diffraction peaks were broad and subtle due to the finite size of the SnO₂ crystallites.^[36] This phenomenon is known as Debye–Scherrer broadening. The XRD pattern of

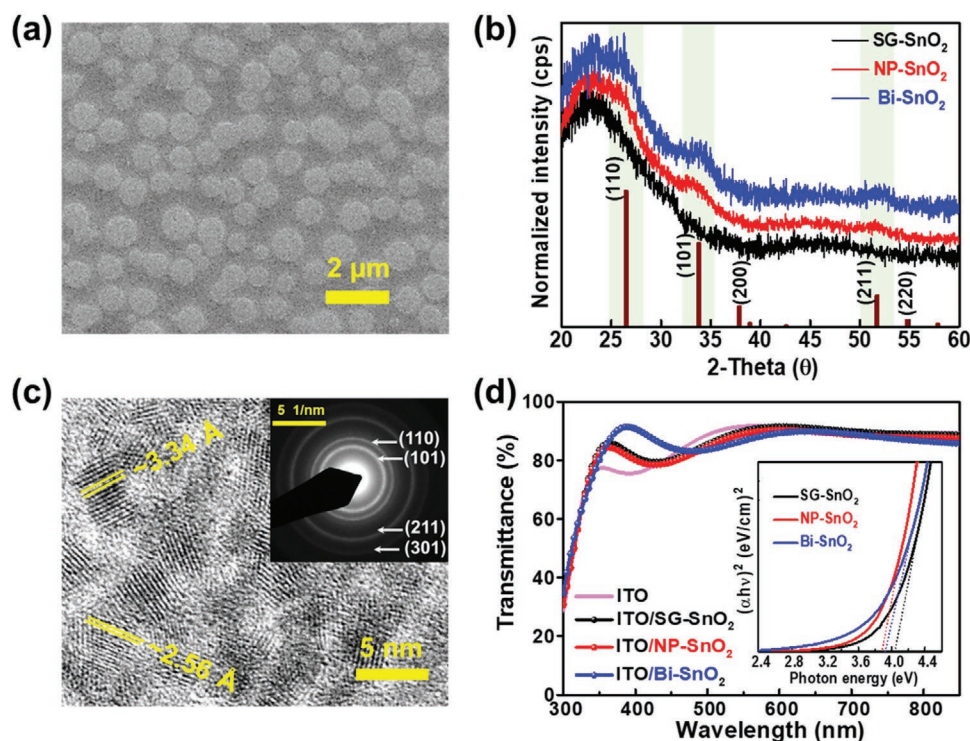


Figure 2. a) Top-view FESEM image of the nanostructured SG-SnO₂ film. b) XRD spectra of the different SnO₂ films. c) HR-TEM micrograph of the SnO₂ colloidal NPs; inset shows the corresponding SAED pattern. d) Optical transmittance of the SnO₂ films deposited on ITO substrate; inset shows the corresponding Tauc plots.

the Bi-SnO₂ film is rather similar with that of the NP-SnO₂ film because it also partially contains SnO₂ colloidal nanoparticles. The subtle diffraction peaks in the XRD patterns of both the NP-SnO₂ and Bi-SnO₂ films at 2θ angles of 26.6°, 33.9°, 38.0°, 51.8°, and 54.8° can be indexed to the (110), (101), (200), (211), and (220) lattice planes, respectively. These peaks indicated that the SnO₂ nanoparticles scaffold exhibit a cassiterite crystal phase with a tetragonal rutile structure (JCPDS card no.: 01-072-1147).^[37] To provide a more in-depth analysis of the crystallography of the SnO₂ colloidal nanoparticles, high-resolution transmission electron microscopy (HRTEM) characterization was conducted. The HRTEM micrograph in Figure 2c illustrates the quasi-spherical morphology of the SnO₂ nanoparticles with a diameter of 4–5 nm. The lattice fringes of the SnO₂ nanoparticles are present at two different d-spacing values, that is, 3.34 and 2.56 Å, which correspond to the (110) and (101) planes of cassiterite SnO₂, respectively. Concurrently, the selected-area electron diffraction (SAED) pattern of the SnO₂ nanoparticles in Figure 2c demonstrates a set of diffraction rings, indicating the polycrystalline nature of the nanoparticles. The diffraction rings can be indexed to the (110), (101), (211), and (301) crystal planes of the cassiterite SnO₂ crystal, which agrees well with the previous XRD findings. Based on the XRD and HRTEM findings, it is conclusive that the SG-SnO₂ film has an amorphous phase, the NP-SnO₂ film has a crystalline phase, and the Bi-SnO₂ film has an amorphous–crystalline heterophase. Furthermore, the optical transmittance of each SnO₂ film was also investigated and the transmittance spectra of the films are presented in Figure 2d. Interestingly, the transmittance of

the Bi-SnO₂ film was not diminished by the insertion of the NP scaffold or its higher thickness. Instead, the Bi-SnO₂ film exhibited the highest transmittance in the UV-range, which is likely due to the stronger light propagation and photon oscillation at the ITO/SnO₂ interface with increasing film thickness.^[38] To further verify this, a simple finite-difference time-domain simulation has been conducted to calculate the optical transmittance spectra of the nanostructured SG-SnO₂, NP-SnO₂, and Bi-SnO₂ films on ITO substrate. The detailed simulation method and input parameters can be found in Supporting Information. The simulation results (Figure S3, Supporting Information) suggest that all SnO₂ films have lower refractive indices than that of the ITO based on volume averaging theory^[39] and act as antireflective layers that lead to enhanced optical transmittance. The simulation results are well in line with the experimental results, confirming the enhanced optical performance of ITO/SnO₂ films from that of the bare ITO. High transmittance is essential for SnO₂ films to ensure maximum light harvesting in the perovskite film. From the Tauc Plot (inset) derived from the absorption spectra of the glass/SnO₂ films, the optical band gaps (E_g) of the SG-SnO₂, NP-SnO₂, and Bi-SnO₂ films were found to be ≈4.02 eV, ≈3.89 eV, and ≈3.93 eV, respectively. The noticeable deviation in E_g implies that there is a significant alteration in the energy band structure of the SnO₂ films following surface modification.

Besides surface morphology and crystallography changes, XPS characterization was conducted to investigate the elemental composition of the SG-SnO₂, NP-SnO₂, and Bi-SnO₂ films. The most noticeable difference in the XPS survey scan

spectra (Figure S4, Supporting Information) is the detection of the Cl element in the SG-SnO₂ film which originates from the use of SnCl₄·2H₂O precursor. For a more in-depth analysis, resolutions of the Sn 3d and O 1s spectra for each SnO₂ film are provided. There are two pronounced peaks observed in the Sn 3d spectra of all SnO₂ films, namely Sn 3d_{5/2} and Sn 3d_{3/2} peaks located at a binding energy (B.E.) of ≈487.3 eV and ≈495.7 eV, respectively (Figure S5, Supporting Information). No visible changes were observed in the Sn 3d spectra despite the morphology and crystallographic changes in the SnO₂ films. However, substantial changes were observed in the O 1s spectra. As displayed in **Figure 3a**, the broad O 1s spectra of all SnO₂ films can be deconvoluted into three Gaussian subpeaks, denoted as O₁ (≈530 eV), O₂ (≈531.5 eV), and O₃ (≈532.5 eV), respectively. The detailed atomic percentages of the deconvoluted O 1s components are presented in Table S2, Supporting Information. Specifically, the dominant O₁ peak located at a lower B.E. can be associated with the O species in the Sn–O bond, whereas the subsidiary O₂ and O₃ peaks located at higher binding energies are commonly assigned to oxygen vacancies (V_O) and dangling hydroxyl (–OH) groups bounded on the SnO₂ surface, respectively.^[40,41] Based on the area under the curve of each O component, the fractions of lattice oxygen atoms (O_{lattice}) and oxygen defects (O_{defect}) in each SnO₂ film were calculated. According to Table S2, Supporting Information, the SG-SnO₂ film exhibited the highest [O_{defect}/O_{lattice}] fraction of ≈0.6592, indicating the abundance of oxygen-related defects in the SG-SnO₂ film surface acquired via the sol–gel method. On the contrary, the Bi-SnO₂ film exhibited the lowest fraction of [O_{defect}/O_{lattice}]

fraction of ≈0.4596, signifying that there are fewer oxygen defects in the film and that the O component arises predominantly from the Sn–O bond. The considerably lower [O_{defect}/O_{lattice}] of the Bi-SnO₂ film originates mainly from the reduction of the surface –OH group (O₃ component). These surface –OH groups and V_O defects could turn into charge recombination centers that hinder the charge carrier transport. Therefore, the significantly fewer O-defects in the Bi-SnO₂ film is highly beneficial for its role as an ETL in PSCs. It is noteworthy that an additional broad shake-up/satellite peak (circled region) was observed in the C 1s spectra of both the NP-SnO₂ and Bi-SnO₂ films (Figure 3d). This satellite peak can be attributed to the presence of the carboxyl group (–COOH) in the ligands of the SnO₂ NPs that caused the sudden emission of photoelectrons during measurement. This particular peak was not observed in the SG-SnO₂ film due to the absence of SnO₂ NPs (ligand host). This finding correlates well with the detection of the additional carboxylic dangling C=O bond (1652 cm^{−1}) and O–H bond (3381 cm^{−1}) in the FT-IR spectra of the NP-SnO₂ and Bi-SnO₂ films (Figure S6, Supporting Information).^[42,43]

Concurrently, UPS measurements were conducted to investigate the quasi-Fermi-level alignments of all SnO₂ films. Figure 3b,c present the UPS spectra of the SnO₂ films in the Fermi edge region and cut-off energy region, respectively. The figures reveal significant alterations in the $E_{\text{cut-off}}$ and $E_{\text{on-set}}$ parameters of the different SnO₂ films and the detailed values of $E_{\text{cut-off}}$ and $E_{\text{on-set}}$ of each SnO₂ film are summarized in Table S3, Supporting Information. Based on Equation (S1),

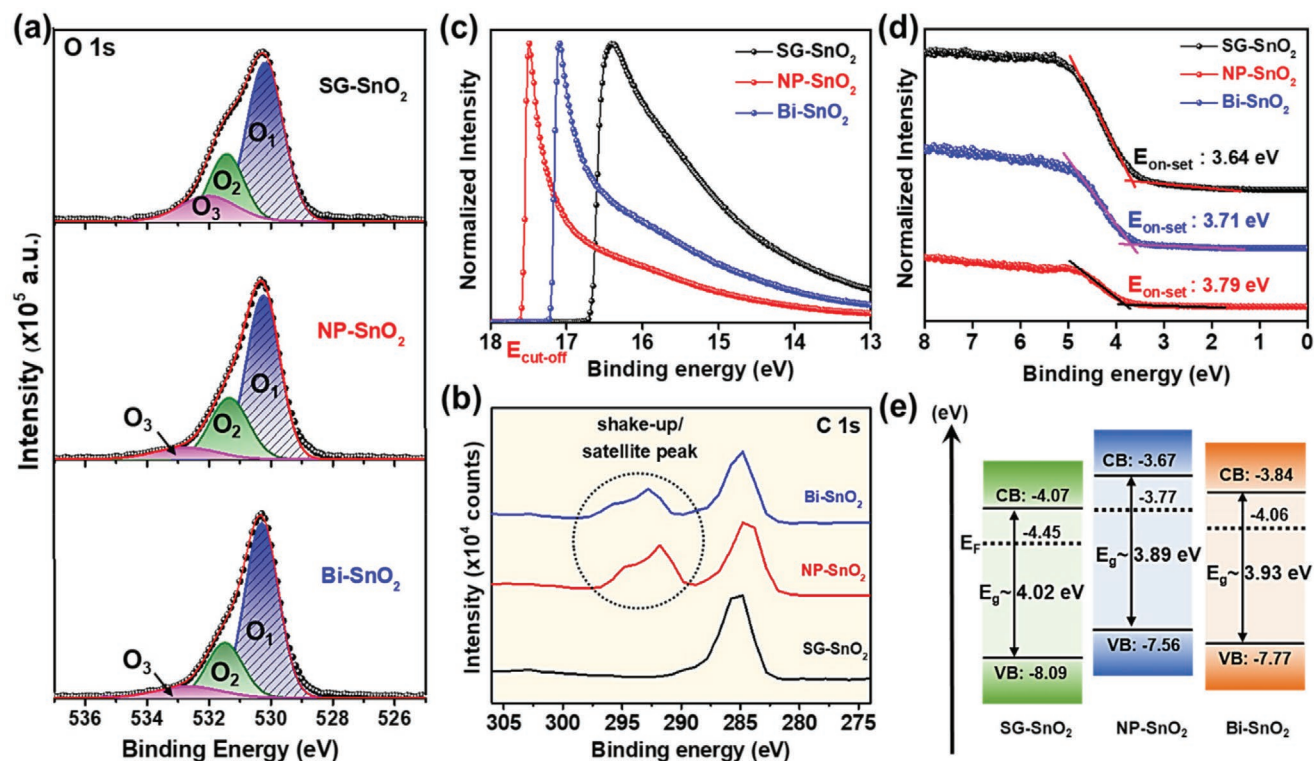


Figure 3. High-resolution a) O 1s and b) C 1s XPS spectra of different SnO₂ films on the ITO glass. c) Cut-off energy region, and d) fermi-edge region of different SnO₂ films on ITO glass obtained from the UPS measurement. e) Schematic energy band structures of SG-SnO₂, NP-SnO₂, and Bi-SnO₂ ETLs.

Supporting Information, the valance band energy levels (E_{VB}) of the SG-SnO₂, NP-SnO₂, and Bi-SnO₂ films were determined to be -8.09, -7.56, and -7.77 eV, respectively. Based on Equation (S2), Supporting Information, the quasi-Fermi energy levels (E_F) of SG-SnO₂, NP-SnO₂, and Bi-SnO₂ films were found to be -4.45, -3.77, and -4.06 eV, respectively. Apparently, there is an upshift in the E_F of the Bi-SnO₂ film with respect to the SG-SnO₂ film, owing to the presence of the overlaying NP scaffold. Based on the value of the E_F obtained from the UPS spectra and the value of E_g derived from the Tauc plot, the energy band diagrams of the three different SnO₂ films are schematically illustrated in Figure 3e. The XPS and UPS results have proven that substantial changes have occurred in the chemical composition and energy band structure of the Bi-SnO₂ film, which can lead to considerable changes in the device performance of PSC.

Next, the photovoltaic performances of the triple-cation PSCs based on SG-SnO₂, NP-SnO₂, and Bi-SnO₂ ETLs were investigated. The device architecture of the PSC is schematically illustrated in Figure 4a. The current density–voltage (J - V) curves of the best PSC devices based on the different SnO₂ ETLs are displayed in Figure 4b and the detailed photovoltaic parameters are summarized in Table 1. The use of SG-SnO₂ and NP-SnO₂ ETLs have yielded comparable device performance in the PSCs, achieving an optimum PCE of $\approx 18.67\%$ and $\approx 18.49\%$, respectively (Table 1). Fascinatingly, the use of the tailored Bi-SnO₂ ETL has contributed to significant V_{oc} , J_{sc} , and FF improvements, thereby elevating the PCE of the PSC up to a maximum of $\approx 20.39\%$. The average photovoltaic parameters

of the different SnO₂-PSC devices are summarized in Table S4, Supporting Information. The corresponding J - V curves under both reverse- and forward-scan directions for each of the PSC devices are displayed in Figure S7, Supporting Information, and the hysteresis index (HI) for each PSC was calculated using Equation (S3), Supporting Information. Apparently, the Bi-SnO₂-based PSC exhibited a much lower HI (≈ 0.009) than those of the SG-SnO₂ (≈ 0.017) and NP-SnO₂ (≈ 0.020) counterparts, which may be ascribed to the improved ETL–perovskite interfacial morphology.

Simultaneously, the external quantum efficiency (EQE) spectra of the different SnO₂-PSC devices are displayed in Figure 4c. The integrated photocurrent density values derived from the EQE spectra are in good accordance with the J_{sc} values obtained from the J - V measurements (Table S5, Supporting Information). The improved performance of the PSC based on the Bi-SnO₂ ETL can be closely associated with the better compatibility of its energy band alignment with that of the triple-cation perovskite film, as depicted in Figure 4d. To explain further, the conduction band level (E_{CB}) of Bi-SnO₂ ETL is higher than that of the SG-SnO₂ ETL and nearer to the E_{CB} of the perovskite film, thus facilitating the extraction of electrons. Similarly, the E_{VB} of the Bi-SnO₂ ETL is deeper than that of the NP-SnO₂ ETL and can, therefore, efficiently prevent the backflow of holes or bimolecular recombination at the ETL/perovskite interface. To further investigate the carrier trap dynamics at ETL/perovskite interface, space-charge-limited current (SCLC) measurements were conducted. For SCLC measurement, electron-only devices with a device architecture

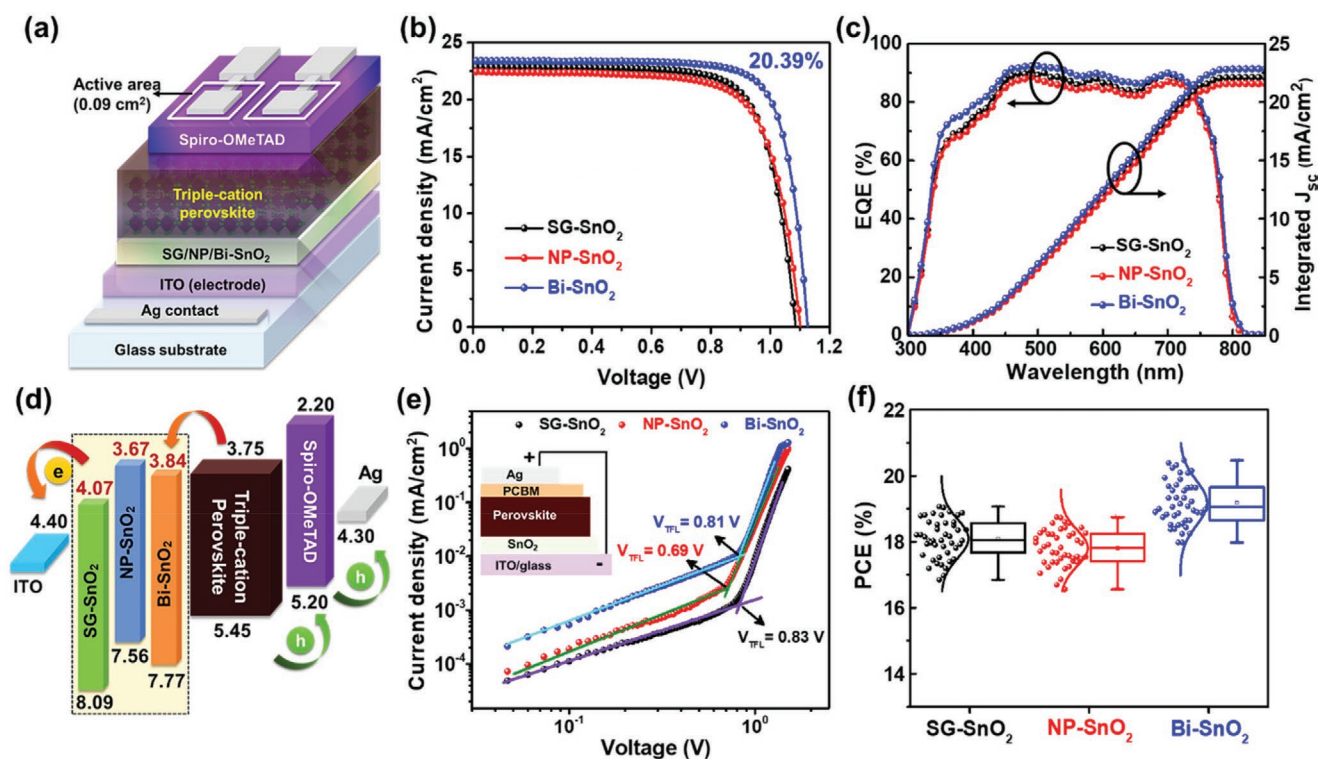


Figure 4. a) Schematic device architecture, b) J - V characteristic curves, c) EQE spectra and the corresponding integrated photocurrent density, d) schematic energy level alignment of PSC devices based on different SnO₂ ETLs. e) SCLC curves of electron-only devices based on different SnO₂ ETLs. f) The PCE distribution of 45 PSC devices based on different SnO₂ ETLs.

Table 1. Photovoltaic parameters of the champion PSC devices based on SG-SnO₂, NP-SnO₂, and Bi-SnO₂ ETLs under one-sun illumination.

PSC device	Scan direction	V _{oc} [V]	J _{sc} [mA cm ⁻²]	FF [%]	PCE [%]	HI
SG-SnO ₂	Reverse	1.088	22.92	74.85	18.67	0.017
	Forward	1.079	22.84	73.57	18.13	
NP-SnO ₂	Reverse	1.109	22.43	74.33	18.49	0.020
	Forward	1.098	22.27	72.81	17.80	
Bi-SnO ₂	Reverse	1.125	23.26	77.92	20.39	0.009
	Forward	1.123	23.12	77.34	20.08	

of ITO/SnO₂/perovskite (500 nm)/PCBM/Ag were fabricated to accurately determine the charge trap densities. The dark J - V characteristic curves of the corresponding SCLC devices are displayed in Figure 4e. From the SCLC plot, the trap density (N_{trap}) and the trap-filled limited voltage (V_{TFL}) can be calculated using Mott-Gurney relation (Equation (S4), Supporting Information). The V_{TFL} values fitted for SG-SnO₂, NP-SnO₂, and Bi-SnO₂ based SCLC devices were 0.83, 0.69, and 0.81 V, respectively. The trap density is directly proportional to the V_{TFL} , therefore, a lower V_{TFL} signifies a lower concentration of trap states. Correspondingly, the calculated N_{trap} values for SG-SnO₂, NP-SnO₂, and Bi-SnO₂-based SCLC devices are 9.2×10^{16} , 7.3×10^{16} , and 7.7×10^{16} cm⁻³, respectively. The NP-SnO₂ device exhibited the lowest trap density, which is attributable to the compact and smooth morphology of the NP-SnO₂ ETL. Similarly, the trap density of the Bi-SnO₂ device is also much lower than that of the SG-SnO₂ device. This phenomenon can be ascribed to the presence of the nanoparticles scaffold in the tailored bilayer structure of Bi-SnO₂ ETL which induced defect-passivation and helped to the roughness of the film surface. The overall N_{trap} trend of the SCLC device is in good correlation with the concentration of O-defects revealed in the XPS result and the PL quenching trend. Low trap density is highly desired in SnO₂ ETL to enable efficient carrier transport in the PSC device. On another note, the PCEs of 45 PSCs based on the different SnO₂ ETLs were statistically analyzed and presented in Figure 4f. The whisker plot demonstrates that the device performance for all SnO₂-PSCs are highly consistent and reproducible. The PCEs of Bi-SnO₂ devices are generally ≈ 1.5 –2% higher than those of the SG-SnO₂ and NP-SnO₂ counterparts.

The device performance of the PSC is closely associated with morphology of the SnO₂ ETLs. Based on the morphology of each SnO₂ film, the ETL/perovskite interfacial morphology of PSCs based on different SnO₂ films are schematically illustrated in Figure 5. In the case of the amorphous SG-SnO₂ ETL (Figure 5a), the formation of the SnO₂ nanodomains with a high surface-to-volume ratio is beneficial for providing larger ETL/perovskite interfacial contact area. This implies that there are more active areas available for charge transfer, which is advantageous for the device performance. Nonetheless, the SG-SnO₂ ETL suffers from a coarse-textured surface and high void density, which may trigger the unwanted collection of holes by the ITO electrode, especially in the void areas where there is a direct contact between the perovskite film and ITO electrode. On the other hand, the crystalline NP-SnO₂ ETL exhibits an ultrasmooth surface and compact morphology, which could effectively provide a direct electron transport pathway and prevent a direct contact between the perovskite film and the ITO electrode, as illustrated in Figure 5b. However, the fine-grained texture of the NP-SnO₂ ETL yields only a limited ETL-perovskite interfacial contact area in comparison with the SG-SnO₂ ETL, leading to less efficient current extraction. From here, it is deducible that the use of the amorphous SG-SnO₂ ETL is likely to yield a higher carrier (electron) concentration due to the larger ETL-perovskite contact, whereas the use of the crystalline NP-SnO₂ ETL is beneficial for carrier (electron) mobility because of the direct charge transport pathway. In this regard, the design of the amorphous-crystalline heterophase Bi-SnO₂ ETL, which retains the morphological features of the individual SG-SnO₂ and NP-SnO₂ ETLs, appears to be the most

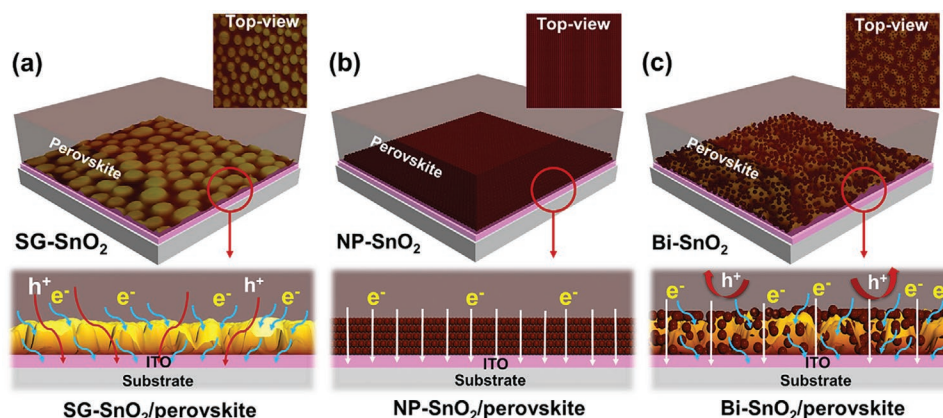


Figure 5. 2D- and 3D- schematic illustration of the charge transfers at ETL/perovskite interface in the PSCs based on a) SG-SnO₂, b) NP-SnO₂, and c) Bi-SnO₂ ETLs.

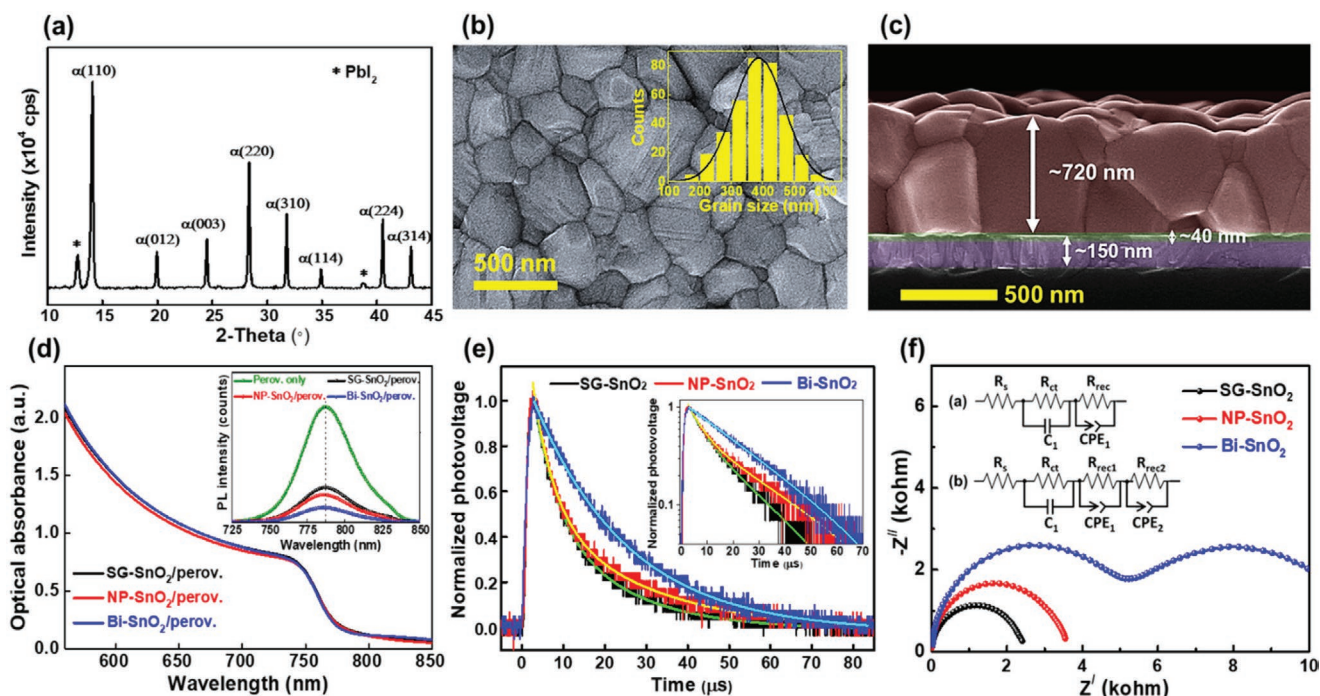


Figure 6. a) XRD pattern, b) top-view FESEM image; histogram plot (inset) shows the grain size distribution, and c) cross-sectional FESEM image of the Bi-SnO₂/perovskite film. d) Optical absorption spectra and steady-state PL spectra (inset) of different SnO₂ ETL/perovskite films. e) Normalized TPV decay curves in linear scale and log scale (inset), f) dark Nyquist plots of PSC devices based on the different SnO₂ ETLs; insets in (a) and (b) represent the equivalent electrical circuits of PSCs based on SG-SnO₂/NP-SnO₂ ETLs and Bi-SnO₂ ETLs, respectively.

practical solution. Bi-SnO₂ ETL provides a much larger ETL/perovskite interfacial area for charge extraction and shields the hole carriers from reaching the ITO electrode more effectively (Figure 5c). This makes Bi-SnO₂ an overall better ETL candidate than both of its predecessors. The higher PCE observed in the Bi-SnO₂-based PSC is ascribable to the improved its ETL/perovskite interfacial morphology.

In conjunction with this, the crystallinity and morphology of the Bi-SnO₂/perovskite film were studied. The XRD patterns in Figure 6a shows that the Bi-SnO₂/perovskite film is highly crystalline in nature and exhibits a dominant (110) peak at a 2θ angle of $\approx 14.1^\circ$. Besides the (110) peak, the other characteristic peaks of triple-cation perovskite, such as (012), (003), (220), (310), (114), (224), and (314) have also been detected. There is also a noticeable peak at the 2θ angle of $\approx 12.7^\circ$ which reflects the presence of the remnant PbI₂ in the perovskite film. The top-view FESEM micrograph in Figure 6b depicts that the Bi-SnO₂/perovskite film is highly compact, pinhole-free and composed of distinguishable grains with an average grain size of ≈ 389 nm (Figure S8, Supporting Information). Based on the cross-section FESEM micrograph in Figure 6c, the thicknesses of the vertically-stacked ITO/Bi-SnO₂/perovskite layers are 150 nm/40 nm/720 nm, respectively. Additionally, a parallel comparison of the XRD patterns and top-view FESEM images of the SG-SnO₂/perovskite and NP-SnO₂/perovskite samples are presented in Figure S9, Supporting Information. Despite the underlying SnO₂ ETLs exhibit distinctively different surface morphologies, there are only negligible changes observed in the morphology and crystallinity of the overlaying perovskite films because the fabrication route of the perovskite films

was the same. Apparently, the morphology of the underlying SnO₂ ETL has no significant influence on the subsequent perovskite film deposition. Next, the optical absorption of the perovskite films deposited on top of the different SnO₂ ETLs were investigated. There are limited changes in the optical absorption of the perovskite films, suggesting that the thickness and light-harvesting efficiency of the perovskite films on the different SnO₂ ETLs are the same (Figure 6d). In parallel with this, a steady-state PL measurement (inset) was conducted to investigate the interfacial charge transfer dynamics of the different SnO₂/perovskite samples. In the presence of SnO₂, the PL emission of the perovskite film quenched significantly as a result of charge transfer at the SnO₂/perovskite interface. Particularly, the PL emission of the perovskite film quenched the most with the use of the Bi-SnO₂, indicating more efficient electron extraction at the Bi-SnO₂/perovskite interface. This improvement can be attributed to the fewer oxygen defects and surface -OH groups in the Bi-SnO₂ ETL, which could turn into deep-level trap states that trigger undesirable carrier recombination. Transient photovoltage (TPV) measurements were conducted to probe the carrier recombination kinetics of and carrier recombination lifetime (τ_{rec}) of the different SnO₂-based PSC devices. The resulting TPV decay profiles are presented in Figure 6e. Apparently, the Bi-SnO₂ device exhibits slower TPV decay and significantly longer τ_{rec} (≈ 22.8 μs) than the SG-SnO₂ ($\tau_{\text{rec}} \approx 15.5$ μs) and NP-SnO₂ ($\tau_{\text{rec}} \approx 18.1$ μs) counterparts. The prolonged τ_{rec} evidences the lesser bimolecular recombination of charge carriers in the Bi-SnO₂ device, which explained its higher V_{oc} compared to the other devices. To further study the charge transfer dynamics of the PSC devices

based on the different SnO_2 ETLs, an electrochemical impedance spectroscopy measurement was conducted under dark condition, applying a 0.9 V bias at room temperature. As displayed in Figure 6f, the Nyquist plots of the SG- SnO_2 - and NP- SnO_2 -based devices show only one visible arc, whereas the Nyquist plot of Bi- SnO_2 comprises two visible arcs. Specifically, the arc at the higher frequency represents the charge transfer resistance (R_{ct}), whereas the arcs at the lower frequency is associated with the charge recombination resistance (R_{rec}) at the interface of the ETL/perovskite that is inversely proportional to the recombination rate of charge carriers. The equivalent electrical circuits for SG- SnO_2 /NP- SnO_2 -based devices and Bi- SnO_2 -based devices are illustrated in insets of Figure 6a,b, respectively. Most noticeably, the electrical equivalent circuit of Bi- SnO_2 device consists of two R_{rec} components, suggesting the existence of an additional charge transfer interface arising from the SG- SnO_2 /NP- SnO_2 bilayer architecture. This additional charge compound resistance is not observed in SG- SnO_2 or NP- SnO_2 devices with single layer architecture. The fitted R_{rec} values for SG- SnO_2 -, NP- SnO_2 -, and Bi- SnO_2 -based devices are 2.32, 3.08, and 5.09 k Ω , respectively. The rest of the fitted parameters can be found in Table S6, Supporting Information. In the case of Bi- SnO_2 , the addition of NPs scaffold on top of the SG- SnO_2 underlayer has effectively reduced the R_{ct} and increased the R_{rec} , indicating more efficient charge extraction, transfer, and less interfacial recombination in the device. All of these factors have substantiated the efficiency improvement in the Bi- SnO_2 device.

As aforementioned, the use of different SnO_2 ETLs have yielded PSC devices with different hysteresis behavior. It has been reported that the hysteresis of the PSC device is in close association with the device stability.^[44,45] To validate this finding, the long-term stabilities of the non-encapsulated and encapsulated PSC devices based on different SnO_2 ETLs were evaluated, and the resulting stability curves are displayed in Figure S10, Supporting Information. In non-encapsulated state, the Bi- SnO_2 -based PSC device which exhibits the lowest hysteresis, is displaying improved long-term stability than the NP- SnO_2 counterpart which suffers from more severe hysteresis. Meanwhile, in encapsulated state, all of the SnO_2 -PSC devices displayed >90% PCE retention after >2000 h of aging in air. Therefore, it is clear that the tailored Bi- SnO_2 bilayer is a more ideal ETL candidate because it yields hysteresis-free PSC with great efficiency and stability.

Furthermore, we also fabricated large-area PSC devices with active areas (A) of 1.15 and 3.55 cm^2 . The surface of the large-area perovskite film exhibits relatively more pinholes and grain boundaries than the small-area (standard) perovskite film (Figure S11, Supporting Information). As a compensation for the increase of series resistance among the charge transport layers, the perovskite absorber layer and the electrode with the increase of cell size, Ag paste subsidiary electrodes were applied on top of the ITO electrode to ensure efficient current collection, as illustrated in Figure 7a. The J - V curves of the large-area (1.15 cm^2 ; 3.55 cm^2) PSCs based on SG- SnO_2 and Bi- SnO_2 are displayed in Figure 7b and 7c, respectively. Based on the results in Table 2,

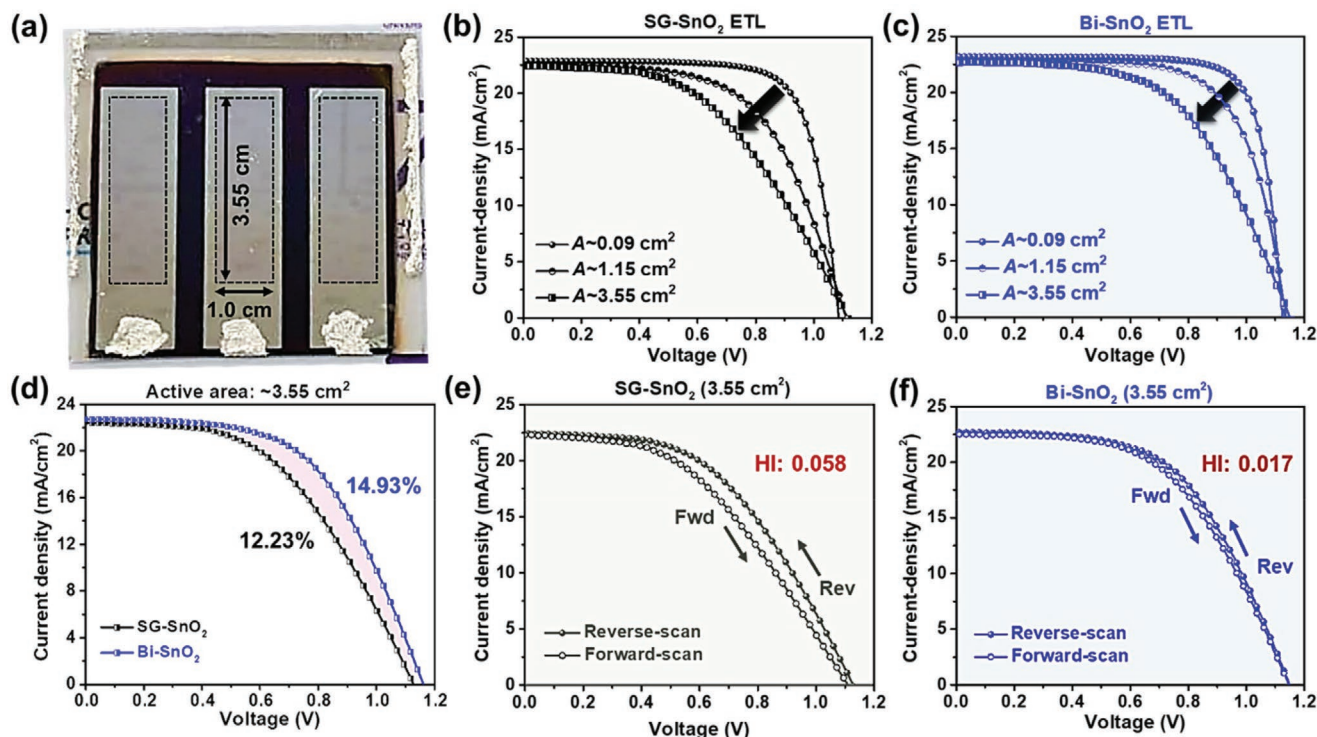


Figure 7. a) Real image of large-area PSCs fabricated on 5 cm \times 5 cm ITO substrate. One substrate can yield up to three devices, each with a defined active area of $\approx 3.55 \text{ cm}^2$. J - V curves of the PSCs with different active areas based on the b) SG- SnO_2 and c) Bi- SnO_2 ETLs. d) PCE disparity between SG- SnO_2 - and Bi- SnO_2 based large-area PSCs ($A \approx 3.55 \text{ cm}^2$). J - V curves under forward- and reverse-scan directions of based large-area PSC devices ($A \approx 3.55 \text{ cm}^2$) based on e) SG- SnO_2 and f) Bi- SnO_2 .

Table 2. Photovoltaic parameters of the large-area PSC devices based on SG-SnO₂ and Bi-SnO₂ ETLs under one-sun illumination.

Active area, A [cm ²]	Scan direction	V _{oc} [V]	J _{sc} [mA cm ⁻²]	FF [%]	PCE [%]	HI	PCE retention [%]
SG-SnO ₂ ETL							
0.09 (small)	Reverse	1.088	22.92	74.85	18.67	0.017	N/A
	Forward	1.079	22.84	73.22	18.04		
1.15 (large)	Reverse	1.113	22.58	58.96	14.82	0.043	79.38
	Forward	1.112	22.46	55.84	13.95		
3.55 (large)	Reverse	1.124	22.42	48.52	12.23	0.058	65.51
	Forward	1.113	22.34	43.52	10.82		
Bi-SnO ₂ ETL							
0.09 (small)	Reverse	1.125	23.26	77.92	20.39	0.009	N/A
	Forward	1.123	23.12	77.34	20.08		
1.15 (large)	Reverse	1.134	22.94	67.36	17.52	0.012	85.92
	Forward	1.135	22.82	65.69	17.03		
3.55 (large)	Reverse	1.149	22.82	56.97	14.93	0.017	73.22
	Forward	1.147	22.67	53.64	13.94		

it is apparent that the Bi-SnO₂-based PSC exhibits considerably greater photovoltaic performance than the SG-SnO₂-based PSC across different active areas. As a comparison, the large-area Bi-SnO₂ device shows a remarkable PCE of 14.93% at an active area of 3.55 cm², whereas the large-area SG-SnO₂ device has a much lower PCE of 12.23% (Figure 7d). Numerically, with increasing A from 0.09 to 3.55 cm², the SG-SnO₂-based PSC shows a PCE retention of ≈65%, whereas the Bi-SnO₂ based PSC shows a PCE retention of ≈73%. One of the factors that contributes to the better device performance of the large-area Bi-SnO₂ device is that there are fewer pinholes in the Bi-SnO₂ ETL due to the presence of the subsidiary NP scaffold layer that fills in the void between the nanodomains, thus effectively reducing the leakage current in the device and leading to a much higher FF. In addition, the surface roughness of the Bi-SnO₂ is also lower than that of the SG-SnO₂ and it is a decisive factor in enabling a more ideal ohmic contact between the perovskite and the ETL, especially for a large-area device. Besides uplifting device performance, an improved ETL/perovskite interfacial morphology also plays an equally significant role in suppressing the hysteresis of the large-area PSCs. As displayed in Figure S12, Supporting Information, large-area PSCs based on Bi-SnO₂ exhibits negligible hysteresis compared to the SG-SnO₂ counterparts. At an A of ≈3.55 cm², large-area PSC based on Bi-SnO₂ ETL only showed HI of ≈0.017, whereas the SG-SnO₂ device recorded a much higher HI of ≈0.058, indicating much lesser charge trapping and de-trapping due to deep level defect states at the ETL-perovskite interface. Consequently, the PCE disparity between the SG-SnO₂- and Bi-SnO₂-based PSCs increased systematically with the device active area, from ≈9.2% (A ≈ 0.09 cm²) of the small-area device to ≈18.2% (A ≈ 1.15 cm²) and ≈22.1% (A ≈ 3.55 cm²) of the large-area device, as shown in Table S7, Supporting Information.

3. Conclusion

This work demonstrates a facile solution route for the fabrication of amorphous–crystalline heterophase Bi-SnO₂ as a highly

efficient ETL for triple-cation PSCs. Compared with the amorphous SG-SnO₂ or the crystalline NP-SnO₂ films, the designed Bi-SnO₂ film exhibited noticeably improved morphology, crystallinity, and optical properties. The void-free morphology, suppressed oxygen defects, and highly compatible energy band alignment of Bi-SnO₂ with that of the perovskite film enabled more efficient electron extraction at the SnO₂-perovskite interface, thereby boosting the PCE of the PSC from ≈18% to more than 20%. The best Bi-SnO₂-based PSC achieved a PCE of ≈20.39%, which is among the highest PCEs obtained for SnO₂-triple cation PSC systems in the literature. More fascinatingly, a large-area PSC (A ≈ 3.55 cm²) based on Bi-SnO₂ ETL has recorded a PCE of ≈14.93%, which is an astounding ≈25% improvement from that of the SG-SnO₂ counterpart. This finding demonstrates that Bi-SnO₂ is a much better ETL than both of its predecessors, especially for the fabrication of a large-area PSC. The low-temperature preparation route of the Bi-SnO₂ PSC holds great promise for applications in the roll-to-roll manufacturing of flexible, large-area PSCs.

4. Experimental Section

Materials: All of the materials, tin(II) chloride dihydrate (SnCl₂·2H₂O, 98%, Sigma-Aldrich), lead(II) iodide (PbI₂, 99.99%, TCI Chemicals), formamidinium iodide (FAI, GreatCell Solar), lead bromide (PbBr₂, >98%, TCI Chemicals), methylammonium bromide (MABr, GreatCell Solar), methylammonium chloride (MACl, Merck), cesium iodide (CsI beads, 99.99%, TCI Chemicals), spiro-oMeTAD (>99%, Lumatech), bis(trifluoromethane)sulfonimide lithium salt (Li-TSFI, 99.95%, Sigma-Aldrich), DMF (99.8%, Sigma-Aldrich), dimethyldimethyl sulfoxide (DMSO, 99.8%, Sigma-Aldrich), ethyl acetate (99.5%, Sigma-Aldrich), hexane (99.5%, Sigma-Aldrich), chlorobenzene (99.9%, Sigma-Aldrich), ethanol (99.5%, Merck), 4-tert-butylpyridine (tBP, 96%, Sigma-Aldrich), and acetonitrile (99.8%, Sigma-Aldrich) were used as received without further purification.

Fabrication of Different SnO₂-Based ETLs: Patterned ITO coated glass substrates (≈10 Ω □⁻¹) with dimensions of 2.5 cm × 2.5 cm were ultrasonically washed in acetone, ethanol, and IPA for 10 min each in sequence and then subjected to UV-ozone treatment for 20 min. Three different kinds of SnO₂ ETLs were prepared in this study, namely

amorphous SG-SnO₂, crystalline NP-SnO₂, and an amorphous–crystalline Bi-SnO₂. The SG-SnO₂ ETL was prepared by spin-coating a precursor solution containing SnCl₂·2H₂O in ethanol (23 mg mL^{−1}) at 3000 rpm for 30 s, followed by annealing treatment at 190 °C in air for an hour. The NP-SnO₂ ETL was prepared by spin-coating the SnO₂ colloidal stock solution (diluted to 2.7 wt% in ultrapure H₂O) at 3000 rpm for 30 s, followed by annealing in air at 150 °C for 30 min. For the fabrication of the Bi-SnO₂ ETL, SG-SnO₂ and NP-SnO₂ were sequentially deposited using the aforementioned spin-coating and annealing condition. The spin-coating speed of SG-SnO₂ and NP-SnO₂ primarily dictated the thickness and subsequent PSC device performance of Bi-SnO₂. Herein, the spin-coating speed of SG-SnO₂ and NP-SnO₂ was fixed at 3000 rpm in the fabrication of Bi-SnO₂ ETL because it yielded the optimum device performance, as summarized in Figure S13 and Table S8, Supporting Information. The SnO₂-coated substrates were then transferred into an N₂ glovebox for further perovskite deposition.

PSC Device Fabrication: The planar PSC devices had a device configuration of ITO/SnO₂/perovskite/Spiro-OMeTAD/Ag. The triple-cation perovskite precursor solution with a general chemical formula of Cs_{0.05}(FAPbI₃)_{0.85}(MAPbBr₃)_{0.15} was prepared by mixing PbI₂ (530 mg), FAI (189 mg), PbBr₂ (75 mg), MABr (18.5 mg), and MACl (4.5 mg) in 1 mL of a DMF:DMSO (4:1 v/v) solvent mixture. Then, 40 µL of a CsI stock solution (1.5 M in DMSO) was added to the precursor solution and the solution was left for overnight stirring in the glove box. The perovskite film was then deposited onto the different SnO₂ ETLs using the one-step antisolvent technique. The green antisolvent used herein was prepared by mixing ethyl acetate (EA) and hexane (Hex) in 7:3 v/v, as reported in the authors' previous work.^[16,46] For the deposition of the perovskite film, 50 µL of the perovskite precursor solution was spin-coated onto the substrate using a two-stage spin-coating program, that is, 1500 rpm for 10 s followed by 5500 rpm for 30 s. At the 10 s interval during the second-stage spin-coating, 100 µL of the EA–Hex mixed antisolvent was continuously dripped onto the spinning substrate. The perovskite films were then annealed at 45 °C for 2 min in the glovebox and a further 150 °C for 20 min in air. Spiro-OMeTAD was deposited onto the perovskite film by spin-coating 30 µL of the mixed solution, which contained 72.3 mg of spiro-OMeTAD salt in 1 mL of CB, doped with 30 µL of 4-tBp, and 35 µL of Li-TSFI solution (260 mg in 1 mL of acetonitrile). Finally, an ≈100 nm Ag contact was thermally evaporated as the top electrode using a shadow mask (aperture area: 0.09 cm²; 1.15 cm²). For the fabrication of large-area PSCs, the SnO₂ ETL (SG-SnO₂ or Bi-SnO₂) was first deposited on the patterned ITO substrate with dimensions of 5 cm × 5 cm, followed by the deposition of the perovskite film in the glovebox using the anti-solvent technique. A total of 400 µL of EA–Hex antisolvent was rapidly dripped onto the spinning substrate. A shadow mask (aperture area ≈ 6.25 cm²) was used for Ag contact evaporation. Another smaller shadow mask (aperture area of 3.55 cm²) was used for the J–V measurement of the large-area PSCs.

Device Characterization: The surface morphology and topography of the different SnO₂ films and perovskite films were investigated using an FESEM (Hitachi SU-70) and an atomic force microscope (Park Systems NX10). The crystallographic changes of the SnO₂ films were characterized by an X-ray diffractometer (Bruker D8 Advance) using CuKα excitation. The optical transmittance and absorption of the SnO₂ films were measured using a UV–vis spectrophotometer (PerkinElmer Lambda 750), and the steady-state photoluminescence spectra of the SnO₂/perovskite samples were obtained from a photoluminescence spectrometer (Horiba FluoroMax-4) at an excitation wavelength of 460 nm. For PSC device characterization, the current density–voltage (J–V) measurements were conducted using a Keithley 2400 source meter under a simulated one-sun illumination (100 mW cm^{−2}; AM 1.5G standard) from an Oriel Sol 3A solar simulator (Newport Inc.). Before conducting the measurements, the system was calibrated against a NREL-certified reference solar cell. The EQE spectra of the PSCs were acquired using an Oriel quantum efficiency measurement device (IQE-200). The TPV measurements were performed using a digital oscilloscope (Siglent, SDS 1302CFL, 300 MHz) and a function generator (Tektronix, AFG3022C) by setting the input impedance of oscilloscope

to 1 MΩ. A white LED was used as biased light and a pulsed blue light (473 nm) generated by a laser diode (CNI laser, MBL-FN-473) was used as a perturbation source.^[46,47] The background signal was set to zero by subtracting the average of the signal measured prior to excitation, and then the transient was fitted with a generic double exponential decay function. Dark impedance spectroscopy measurements were carried out using an impedance analyzer (CompactStat, IVIUM Tech) at voltage bias of 0.9 V and a perturbation voltage of 10 mV. The resulting Nyquist plots were fitted using ZView software (Scribner Associates).^[48]

Supporting Information

Supporting Information is available from the Wiley Online Library or from the author.

Acknowledgements

This work was financially supported by the Basic Science Research Program (NRF-2017R1A2B2001838 and NRF-2019R1I1A1A01053127) through the National Research Foundation (NRF) of Korea, funded by the Ministry of Science, ICT and Future Planning.

Conflict of Interest

The authors declare no conflict of interest.

Keywords

band alignment, defects, morphology, ohmic contact, tin oxide

Received: February 18, 2020

Revised: March 27, 2020

Published online:

- [1] Q. Jiang, L. Zhang, H. Wang, X. Yang, J. Meng, H. Liu, Z. Yin, J. Wu, X. Zhang, J. You, *Nat. Energy* **2017**, *2*, 16177.
- [2] Q. Jiang, Y. Zhao, X. Zhang, X. Yang, Y. Chen, Z. Chu, Q. Ye, X. Li, Z. Yin, J. You, *Nat. Photonics* **2019**, *13*, 460.
- [3] Best Research-Cell Efficiency Chart, <https://www.nrel.gov/pv/assets/pdfs/best-research-cell-efficiencies.20200203.pdf> (accessed: February 2020).
- [4] S. S. Shin, J. H. Suk, B. J. Kang, W. Yin, S. J. Lee, J. H. Noh, T. K. Ahn, F. Rotermund, I. S. Cho, S. Il Seok, *Energy Environ. Sci.* **2019**, *12*, 958.
- [5] L. Huang, D. Zhang, S. Bu, R. Peng, Q. Wei, Z. Ge, *Adv. Sci.* **2020**, *7*, 1902656.
- [6] Z. Liu, K. Deng, J. Hu, L. Li, *Angew. Chem.* **2019**, *131*, 11621.
- [7] Y. Zhu, K. Deng, H. Sun, B. Gu, H. Lu, F. Cao, J. Xiong, L. Li, *Adv. Sci.* **2018**, *5*, 1700614.
- [8] L. Etgar, P. Gao, Z. Xue, Q. Peng, A. K. Chandiran, B. Liu, M. K. Nazeeruddin, M. Grätzel, *J. Am. Chem. Soc.* **2012**, *134*, 17396.
- [9] W. Ke, G. Fang, J. Wang, P. Qin, H. Tao, H. Lei, Q. Liu, X. Dai, X. Zhao, *ACS Appl. Mater. Interfaces* **2014**, *6*, 15959.
- [10] T. Leijtens, G. E. Eperon, S. Pathak, A. Abate, M. M. Lee, H. J. Snaith, *Nat. Commun.* **2013**, *4*, 2885.
- [11] J. Ma, Z. Lin, X. Guo, L. Zhou, J. Su, C. Zhang, Z. Yang, J. Chang, S. Frank Liu, Y. Hao, *Sol. RRL* **2019**, *3*, 1900096.

- [12] C. Chen, Y. Jiang, Y. Wu, J. Guo, X. Kong, X. Wu, Y. Li, D. Zheng, S. Wu, X. Gao, Q. Wang, G. Zhou, Y. Chen, J.-M. Liu, K. Kempa, J. Gao, *Sol. RRL* **2020**, 4, 1900499.
- [13] C. Zhang, Y. Shi, S. Wang, Q. Dong, Y. Feng, L. Wang, K. Wang, Y. Shao, Y. Liu, S. Wang, *J. Mater. Chem. A* **2018**, 6, 17882.
- [14] X. Wang, L.-L. Deng, L.-Y. Wang, S.-M. Dai, Z. Xing, X.-X. Zhan, X.-Z. Lu, S.-Y. Xie, R.-B. Huang, L.-S. Zheng, *J. Mater. Chem. A* **2017**, 5, 1706.
- [15] Q. Luo, H. Chen, Y. Lin, H. Du, Q. Hou, F. Hao, N. Wang, Z. Guo, J. Huang, *Adv. Funct. Mater.* **2017**, 27, 1702090.
- [16] H. B. Lee, M. Jeon, N. Kumar, B. Tyagi, J.-W. Kang, *Adv. Funct. Mater.* **2019**, 29, 1903213.
- [17] X. Yu, S. Chen, K. Yan, X. Cai, H. Hu, M. Peng, B. Chen, B. Dong, X. Gao, D. Zou, *J. Power Sources* **2016**, 325, 534.
- [18] L. Zuo, H. Guo, D. W. DeQuilettes, S. Jariwala, N. de Marco, S. Dong, R. DeBlock, D. S. Ginger, B. Dunn, M. Wang, Y. Yang, *Sci. Adv.* **2017**, 3, e1700106.
- [19] J. Xie, K. Huang, X. Yu, Z. Yang, K. Xiao, Y. Qiang, X. Zhu, L. Xu, P. Wang, C. Cui, D. Yang, *ACS Nano* **2017**, 11, 9176.
- [20] Z. Wang, Q. Lin, F. P. Chmiel, N. Sakai, L. M. Herz, H. J. Snaith, *Nat. Energy* **2017**, 2, 17135.
- [21] E. H. Anaraki, A. Kermanpur, L. Steier, K. Domanski, T. Matsui, W. Tress, M. Saliba, A. Abate, M. Grätzel, A. Hagfeldt, J.-P. Correa-Baena, *Energy Environ. Sci.* **2016**, 9, 3128.
- [22] Y. Chen, Q. Meng, L. Zhang, C. Han, H. Gao, Y. Zhang, H. Yan, *J. Energy Chem.* **2019**, 35, 144.
- [23] X. Zhao, S. Liu, H. Zhang, S. Chang, W. Huang, B. Zhu, Y. Shen, C. Shen, D. Wang, Y. Yang, M. Wang, *Adv. Funct. Mater.* **2019**, 29, 1805168.
- [24] M. Park, J.-Y. Kim, H. J. Son, C.-H. Lee, S. S. Jang, M. J. Ko, *Nano Energy* **2016**, 26, 208.
- [25] L. Xiong, M. Qin, G. Yang, Y. Guo, H. Lei, Q. Liu, W. Ke, H. Tao, P. Qin, S. Li, H. Yu, G. Fang, *J. Mater. Chem. A* **2016**, 4, 8374.
- [26] E. H. Anaraki, A. Kermanpur, M. T. Mayer, L. Steier, T. Ahmed, S. H. Turren-Cruz, J. Seo, J. Luo, S. M. Zakeeruddin, W. R. Tress, T. Edvinsson, M. Grätzel, A. Hagfeldt, J. P. Correa-Baena, *ACS Energy Lett.* **2018**, 3, 773.
- [27] H. Ye, Z. Liu, X. Liu, B. Sun, X. Tan, Y. Tu, T. Shi, Z. Tang, G. Liao, *Appl. Surf. Sci.* **2019**, 478, 417.
- [28] Y. W. Noh, J. H. Lee, I. S. Jin, S. H. Park, J. W. Jung, *Nano Energy* **2019**, 65, 104014.
- [29] G. Yang, H. Lei, H. Tao, X. Zheng, J. Ma, Q. Liu, W. Ke, Z. Chen, L. Xiong, P. Qin, Z. Chen, M. Qin, X. Lu, Y. Yan, G. Fang, *Small* **2017**, 13, 1601769.
- [30] S. Song, G. Kang, L. Pyeon, C. Lim, G.-Y. Lee, T. Park, J. Choi, *ACS Energy Lett.* **2017**, 2, 2667.
- [31] X. Liu, T. Bu, J. Li, J. He, T. Li, J. Zhang, W. Li, Z. Ku, Y. Peng, F. Huang, Y.-B. Cheng, J. Zhong, *Nano Energy* **2018**, 44, 34.
- [32] Y. Lee, S. Paek, K. T. Cho, E. Oveisi, P. Gao, S. Lee, J.-S. Park, Y. Zhang, R. Humphry-Baker, A. M. Asiri, M. K. Nazeeruddin, *J. Mater. Chem. A* **2017**, 5, 12729.
- [33] X. Liu, T. Bu, J. Li, J. He, T. Li, J. Zhang, W. Li, Z. Ku, Y. Peng, F. Huang, Y.-B. Cheng, J. Zhong, *Nano Energy* **2018**, 44, 34.
- [34] D. Wang, C. Wu, W. Luo, X. Guo, B. Qu, L. Xiao, Z. Chen, *ACS Appl. Energy Mater.* **2018**, 1, 2215.
- [35] J. Ma, G. Yang, M. Qin, X. Zheng, H. Lei, C. Chen, Z. Chen, Y. Guo, H. Han, X. Zhao, G. Fang, *Adv. Sci.* **2017**, 4, 1700031.
- [36] J. Gong, X. Wang, X. Fan, R. Dai, Z. Wang, Z. Zhang, Z. Ding, *Opt. Mater. Express* **2019**, 9, 3691.
- [37] A. Debatara, D. W. Zuhlendri, B. Yulianto, Nugraha, H., B. Sunendar, *Proc. Eng.* **2017**, 170, 60.
- [38] Y. Luan, X. Yi, P. Mao, Y. Wei, J. Zhuang, N. Chen, T. Lin, C. Li, J. Wang, *iScience* **2019**, 16, 433.
- [39] A. Garahan, L. Pilon, J. Yin, I. Saxena, *J. Appl. Phys.* **2007**, 101, 014320.
- [40] X. Wang, Q. Di, X. Wang, H. Zhao, B. Liang, J. Yang, *Mater. Sci. Eng., B* **2019**, 250, 114433.
- [41] H. B. Lee, R. T. Ginting, S. T. Tan, C. H. Tan, A. Alshamleh, H. F. Olewi, C. C. Yap, M. H. H. Jumali, M. Yahaya, *Sci. Rep.* **2016**, 6, 32645.
- [42] Y. Ju, S. Y. Park, H. S. Han, H. S. Jung, *RSC Adv.* **2019**, 9, 7334.
- [43] A. Thote, I. Jeon, H.-S. Lin, S. Manzhos, T. Nakagawa, D. Suh, J. Hwang, M. Kashiwagi, J. Shiomi, S. Maruyama, H. Daiguji, Y. Matsuo, *ACS Appl. Electron. Mater.* **2019**, 1, 389.
- [44] N. Ahn, K. Kwak, M. S. Jang, H. Yoon, B. Y. Lee, J.-K. Lee, P. V. Pikhitsa, J. Byun, M. Choi, *Nat. Commun.* **2016**, 7, 13422.
- [45] N. Ahn, I. Jeon, J. Yoon, E. I. Kauppinen, Y. Matsuo, S. Maruyama, M. Choi, *J. Mater. Chem. A* **2018**, 6, 1382.
- [46] N. Kumar, H. B. Lee, S. Hwang, J.-W. Kang, *J. Mater. Chem. A* **2020**, 8, 3357.
- [47] R. T. Ginting, E.-S. Jung, M.-K. Jeon, W.-Y. Jin, M. Song, J.-W. Kang, *Nano Energy* **2016**, 27, 569.
- [48] R. T. Ginting, M. K. Jeon, K. J. Lee, W. Y. Jin, T. W. Kim, J.-W. Kang, *J. Mater. Chem. A* **2017**, 5, 4527.